Journal of Colloid and Interface Science 454 (2015) 192–199

Contents lists available at ScienceDirect

Journal of Colloid and Interface Science

www.elsevier.com/locate/jcis

Asymmetric capillary bridges between contacting spheres

Timothy P. Farmer, James C. Bird *

Department of Mechanical Engineering, Boston University, Boston, MA 02215, United States

GRAPHICAL ABSTRACT

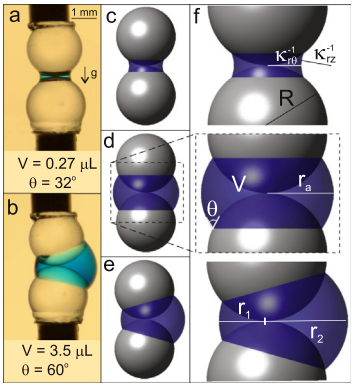

ARTICLE INFO

Article history:
Received 8 January 2015
Accepted 22 April 2015
Available online 19 May 2015

Keywords:
Capillary bridge
Surface energy minimization

ABSTRACT

When a drop of liquid wets two identical solid spheres, the liquid forms a capillary bridge between the spheres to minimize surface energy. In the absence of external forces, these bridges are typically assumed to be axisymmetric, and the shape that minimizes surface energy can be calculated analytically. However under certain conditions, the bridge is axisymmetrically unstable, and migrates to a non-axisymmetric configuration. The goal of this paper is to characterize these non-axisymmetric capillary bridges. Specifically, we numerically calculate the shape of the capillary bridge between two contacting spheres that minimizes the total surface energy for a given volume and contact angle and compare to experiments. When the bridge is asymmetric, finite element calculations demonstrate that the shape of the bridge is spherical. In general, the bridge shape depends on both volume and contact angle, yet we find the degree of asymmetry is controlled by a single parameter.

1. Introduction

When a small amount of liquid wets two identical solid spheres, the liquid will typically form a meniscus, or capillary bridge, between the spheres. Provided that bridge is sufficiently small, gravitational effects are negligible, and the liquid is drawn to the axis of the spheres to minimize surface energy. Extensive research has been carried out to characterize capillary bridges, both because of the elegance of the mathematics [1,2] and because of their importance to a variety of processes in physics and engineering [3–6]. Capillary bridges are important to granular and suspension rheology [7,8]. They trap liquids and gases in soil [9,10] and porous rock [11], as well as influence the adhesion of pharmaceutical powders [12] and sandcastles [13,14]. Yet, almost all studies of capillary bridges between spheres have restricted their analysis to situations in which the bridges are axisymmetric [15–21]. Of the few studies that have pointed out the existence of asymmetric

* Corresponding author.
E-mail address: jbird@bu.edu (J.C. Bird).

http://dx.doi.org/10.1016/j.jcis.2015.04.045
0021-9797/

capillary bridges between spherical particles [22,23], there is an indication that these bridges might adopt a spherical shape; yet the authors were careful not to claim that the asymmetrical spherical bridge indeed minimized surface energy.

The shape of both an axisymmetric and non-axisymmetric capillary bridge can be demonstrated experimentally (Fig. 1a and b). Two glass spheres are adhered to needles and brought to contact. Water, dyed blue, is injected on the spheres and forms a capillary bridge between the spheres and the surrounding air. An axisymmetric capillary bridge forms between the spheres (radius $R = 1$ mm) when the water volume is $V = 0.27$ μL and the apparent contact angle is $\theta = 32°$ (Fig. 1a). As will be described further in the method's section, the particular contact angle is achieved by vapor-depositing a layer of (3-mercatopropyl)trimethoxysilane onto the glass spheres prior to assembly. Above a critical drop volume and apparent contact angle, however, the capillary bridge spontaneously breaks axial symmetry and bulges to one side (Fig. 1b). The goal of this paper is to numerically calculate the shape of bridges that minimize the surface energy for various combinations of volume and contact angle.

In the absence of external forces, the liquid bridge will rearrange until it locally minimizes the cumulative surface energy of each of the interfaces. When a liquid, gas, and solid phase are present, the total surface energy can be expressed as $E = \gamma_{LG}A_{LG} + \gamma_{SG}A_{SG} + \gamma_{SL}A_{SL}$, as there are three distinct interfaces (liquid–gas, solid–gas, and solid–liquid) each with their own interfacial tension γ and surface area A. In the absence of any roughness or chemical heterogeneities, the relative strengths of the surface energies manifest themselves through the equilibrium contact angle θ_{eq} that the three phases make when they meet, following Young's relation [4]: $(\gamma_{SG} - \gamma_{SL})/\gamma_{LG} = \cos\ \theta_{eq}$. In practice, microscopic heterogeneities can be significant and the angle macroscopically observed, referred to here as the apparent contact angle, can deviate from the equilibrium value [24,25]. In addition, the apparent contact angle can modulate between values adopted when the contact line is quasi-statically receding and when the contact line is quasi-statically advancing, a phenomenon referred to as contact angle hysteresis [26,27]. Although the experimental system in Fig. 1 exhibits contact angle hysteresis, the analysis in this paper demonstrates that hysteresis is not necessary to adopt an asymmetric capillary bridge. In this paper, we will refer to the fluid that forms the capillary bridge as a liquid and the surrounding fluid as a gas to be consistent with Fig. 1. However, it should be noted that the analysis presented here does not restrict these phases to be liquid and gas respectively, but rather generalizes to any two immiscible fluids.

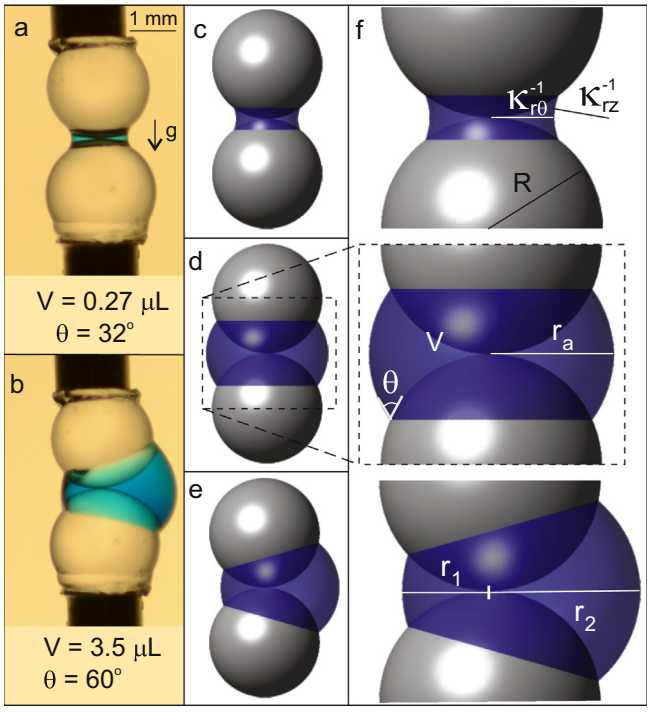

Fig. 1. Experiments and simulations illustrating axisymmetric and asymmetric morphologies. (a) A photograph of 0.27 μL of water wetting two glass spheres with contact angle $\theta = 32°$. (b) At an increased volume ($V = 3.5$ μL) and contact angle ($\theta = 60°$), the water adopts a non-axisymmetric topology. (c) Minimal energy surface simulated for conditions in part a. (d) Axisymmetric minimal energy surface simulated for conditions in part b. (e) Stable minimal energy surface simulated for conditions in part b. (f) Identification of parameters measured from the simulations.

The topological transition illustrated in Fig. 1a and b is reminiscent of the non-axisymmetric instability observed when a drop is squeezed between two parallel disks [28–30]. In that scenario, the capillary bridge adopts a rotund shape and breaks symmetry when the free surface is tangent to the flat surface of the disk. Yet, the contact line on the parallel disks is pinned, whereas on the spheres we will assume that it is free to move along the surface.

Therefore, a closer analogy to the shape transition (Fig. 1a and b) might be the roll-up process of a drop on a cylinder [31–35]. Depending on the contact angle and the volume, a drop will spread around a long cylinder in a shape resembling a barrel shape or alternatively roll-up into a non-axisymmetric shape resembling a clamshell. The drop and cylinder geometries provide a seemingly simple system; yet, even though the morphologies have been calculated numerically [33–35], the precise instability criterion and non-axisymmetric topology are still uncertain [35]. A challenge is the existence of metastable states in which a drop can conform to a topology that is a local energy minimum while not necessarily being a global minimum. The double-sphere geometry (Fig. 1) may be a simpler system to characterize non-axisymmetric bridge morphologies due to rotational symmetries. Yet, as far as we are aware, the stable, non-axisymmetric topologies for drops on the double-sphere geometry have not been calculated analytically or numerically.

In the following sections, we describe our procedure to model the capillary bridge between identical spheres both experimentally (Fig. 1a and b) and numerically (Fig. 1c–e) for a given liquid volume V and contact angle θ. From the finite element calculations, we measure the principle curvatures κ_{rz} and $\kappa_{r\theta}$, as well as the minimum r_1 and maximum r_2 extent of the bridge from the point of contact (Fig. 1f). These parameters are collected for various combinations of volume and contact angle and form the basis of our analysis.

2. Methods

2.1. Experimental methods

To obtain the images in Fig. 1a and b, borosilicate glass beads with a diameter of 2 mm are adhered to the tip of 16 gauge needles. The beads are coated with (3-mercatopropyl) trimethoxysilane by chemical vapor deposition under low pressure so that they are partially wetting. Once coated, the needles are mounted vertically so that the glass beads can be aligned and brought into contact by articulating a 3D stage. Water, dyed blue, is injected between to form a capillary bridge between the separated spheres.

For small volumes, the capillary bridge remains axisymmetric when the glass beads are brought into contact. In these cases only a single photograph is taken. For larger volumes, however, the bridge becomes non-axisymmetric as the beads are drawn together. In these cases, a second photo is taken while the beads

are separated and the capillary bridge is axisymmetric. The volume of the axisymmetric capillary bridge is calculated from the photograph using a custom MATLAB image processing script. The contact angle is measured from the bridge profile when the spheres have contacted (Fig. 1a and b), as are the principle radii r_1 and r_2.

2.2. Numerical methods

We calculate the capillary bridge shape for a given liquid volume and contact angle numerically using Surface Evolver [36,37], a finite element solver. Surface Evolver is designed to minimize the energy of a surface down to an arbitrary level of refinement. To control the shape of the capillary surface, we specify an equilibrium contact angle θ_{eq} via the relative interfacial surface tensions on the different interfaces, as well as a dimensionless volume V/R^3, where R is the radius of the solid spheres.

In our system, the liquid–gas interface is free to deform, whereas the solid–liquid and solid–gas interfaces are constrained to lie on the interface of the solid spheres. In Surface Evolver, facets comprising a constrained surface are especially sensitive to many of the built-in commands that refine and evolve. In lieu of these facets, a path integral is used to calculate their contribution to the total surface energy and volume. Using the documentation as a guide [33], we obtain path integrals accounting for the volume and surface area contributed by the upper and lower spheres:

$$V_{upper} = \oint_{\partial S} \left[\frac{z(3R-2z)}{6(2R-z)}\left(y\vec{i} - x\vec{j}\right)\right]\cdot d\vec{l};$$
$$A_{upper} = \oint_{\partial S} \left[\frac{R}{2R-z}\left(-y\vec{i} + x\vec{j}\right)\right]\cdot d\vec{l} \quad (1)$$

$$V_{lower} = \oint_{\partial S} \left[\frac{z(3R+2z)}{6(2R+z)}\left(y\vec{i} - x\vec{j}\right)\right]\cdot d\vec{l};$$
$$A_{lower} = \oint_{\partial S} \left[\frac{R}{2R+z}\left(-y\vec{i} + x\vec{j}\right)\right]\cdot d\vec{l} \quad (2)$$

The results of this simulation are quite sensitive to the accuracy of these path integrals. Therefore, we verify the path integral simulation by comparing it to a simulation that excludes these elements (Fig. 2). Both simulations are run with the same initial conditions and to the same tolerance at the same maximum level of refinement. The result of the free interface shape using the path integrals (Fig. 2b) is indistinguishable to the shape when facets are used to account for the volume and surface area of the bounding spheres (Fig. 2a). The difference between the images is the facets that would otherwise be constrained to the surfaces of the spheres, and therefore we conclude that the path integrals are implemented correctly.

The procedure to carry out these simulations is illustrated in Fig. 3. An initial axisymmetric profile is defined about the origin with a specified volume (Fig. 3a). This surface is refined and evolved until it reaches an equilibrium shape (Fig. 3b). This shape corresponds to an axisymmetric minimum surface energy configuration of the liquid bridge given the volume, contact angle, and solid boundary constraints. Note that the configuration in Fig. 3b will always be axisymmetric because the initial conditions and perturbations are axisymmetric. Thus, we next introduce non-axisymmetric perturbations. If the axisymmetric bridge configuration is stable, it will return to axisymmetric configuration. Otherwise, the bridge shape will further evolve into a new, stable non-axisymmetric configuration (Fig. 3c).

Simulations are run for more than 2500 unique combinations of contact angle θ_{eq} and dimensionless bridge volume V/R^3. The results of each simulation, a triangular mesh of the bridge profile, are exported to MATLAB. Once imported, custom MATLAB scripts slice the triangular mesh into two-dimensional sections along two independent planes of symmetry. A circular regression [38] is used on these slices to determine r_1, r_2, κ_{rz} and $\kappa_{r\theta}$.

3. Results and discussion

Provided that the fluid is static and the effects of gravity are negligible, the pressure both inside and outside the capillary bridge must be constant. However, because of the curvature of the bridge, these pressures are not necessary the same. The pressure jump across the interface, known as the Laplace pressure, is proportional to the mean curvature. Therefore the shape of the bridge that minimizes surface energy must belong to the class of

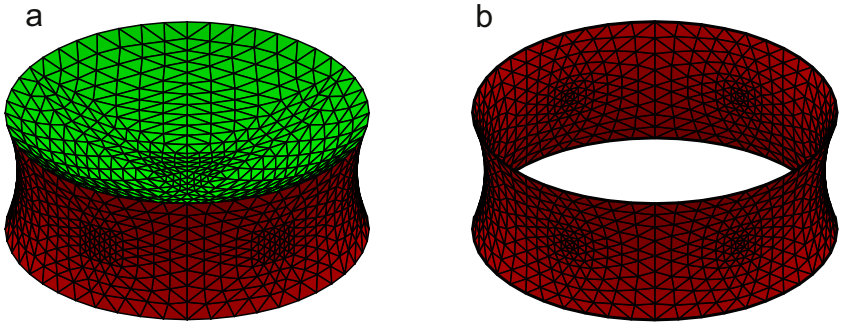

Fig. 2. Verification of surface evolver simulation implementing path integrals. (a) Simulation results when facets (top surface) are used to account for volume and surface area contributed by bounding spheres. (b) Simulation results when path integrals are used to account for volume and surface area contributed by bounding spheres.

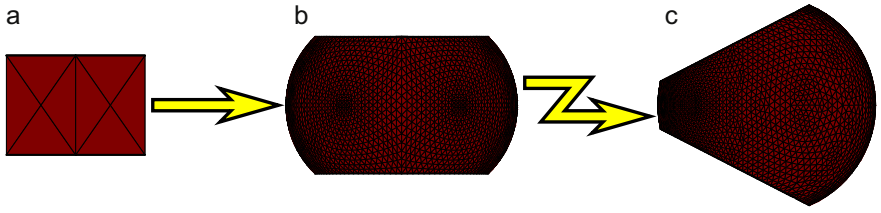

Fig. 3. Typical evolution of a non-axisymmetric capillary bridge. (a) The initial surface is defined. (b) The surface is refined and evolved without additional perturbation until it reaches an equilibrium shape. (c) The surface is perturbed and evolved until it reaches a new, stable equilibrium shape.

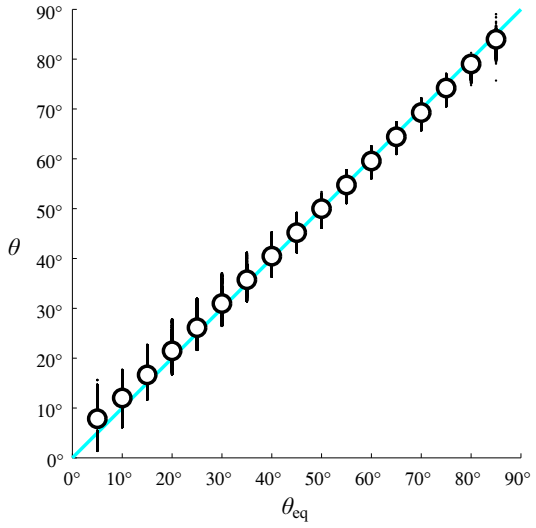

Fig. 4. Apparent contact angle measured from the simulation results as a function of the specified equilibrium contact angle θ_{eq}. From theoretical considerations, it is expected that the apparent and equilibrium contact angles should be equivalent (solid line). The black points are simulation results, with the white circles depicting the mean apparent angle for each equilibrium angle.

constant-mean-curvature surfaces, sometimes referred to as Delaunay surfaces.

The constant mean curvature of the bridge continues as it meets the solid double-sphere surface forming at an apparent contact angle θ at the triple line. Therefore if the bridge is axisymmetric, the apparent contact angle and bridge volume are sufficient to determine the bridge shape, regardless of the physics responsible for the apparent contact angle observed. In the absence of any contact angle hysteresis or microscopic heterogeneities, the apparent contact angle takes the value of the equilibrium contact angle θ_{eq}. This equality has been proved formally for arbitrary axisymmetric geometries by casting the energy minimization as a variational problem and imposing the tranversality condition [39]. Indeed, the apparent contact angles in our simulations are consistent with this result.

Multiple simulations illustrate the one-to-one relationship between the apparent contact angle θ and specified equilibrium contact angle θ_{eq} (Fig. 4). Small circles denote observed contact angles computed from the intersection of contact-line facets and their corresponding spheres (approximately 800,000 points from the 2550 runs). Large circles denoting mean values of these observed contact angles closely match the expected one-to-one relationship between the observed and specified contact angles (solid line).

Because the equivalence of the equilibrium and apparent contact angles in our simulations, we will no longer differentiate them in this manuscript and refer to them both as the contact angle θ. We expect that all of our results equally apply when microscopic heterogeneities are present, provided that contact angle is not pinned and thus free to move along the surface. In these instances, the apparent contact angle may not be the thermodynamic equilibrium contact angle, but acts as an equivalent equilibrium contact angle in constraining the bridge shape.

By setting the volume and contact angle to be equivalent to the experiment in Fig. 1a and minimizing the surface energy, the theoretical bridge shape is computed (Fig. 1c). The experimentally observed shape (Fig. 1a) is similar to the simulation (Fig. 1c), confirming that gravity and other external forces are indeed negligible.

When simulations are carried out with the volume and contact angle to be equivalent to the experiment in Fig. 1b, the axisymmetric configuration that minimizes surface energy (Fig. 1d) is noticeably different than the experimentally observed shape (Fig. 1b). Furthermore, when the non-axisymmetric perturbations are introduced, the simulated bridge shifts to an asymmetric configuration (Fig. 1e) that is qualitatively similar to the experimentally observed shape (Fig. 1b).

The experimental observations and computations suggest that there must be critical states of volume and contact angle that separate the axisymmetric and non-axisymmetric configurations. Setting an origin at the contact point of the spheres, we record the minimum radius r_1 and maximum radius r_2 in the plane of symmetry (Fig. 1f). If the bridge is axisymmetric, the minimum and maximum radii are equivalent and equal to the axisymmetric radius r_a. By carrying out numerous independent simulations, we systematically compute these radii for different volume and contact angle combinations.

Starting with the constraints in Fig. 1b (dotted-dashed lines in Fig. 5), the simulations suggest that the non-axisymmetric bridge would become axisymmetric if either the volume were decreased (Fig. 5a) or the contact angle decreased (Fig. 5b). There is a distinct bifurcation point where the axisymmetric bridge transitions from being stable to unstable (Fig. 5a, dashed lines). Here the radii and volume are non-dimensionalized by the radius of the solid spheres R.

The overall stability is illustrated by plotting the ratio r_1/r_2 as a function of the volume and contact angle (Fig. 6). The bridge is axisymmetric when $r_1/r_2 = 1$ and non-axisymmetric for all other values. The simulations demonstrate that the ratio is equal to one when the volume and contact angle are sufficiently small and monotonically decreases as the volume and contact angles increase. Although these results are sufficient to tabulate the degree of asymmetry, they do not provide a deep understanding as to why this asymmetry develops.

In addition to the minimum and maximum bridge radius, we also calculate the principle curvatures $\kappa_{r\theta}$ and κ_{rz} of the simulated

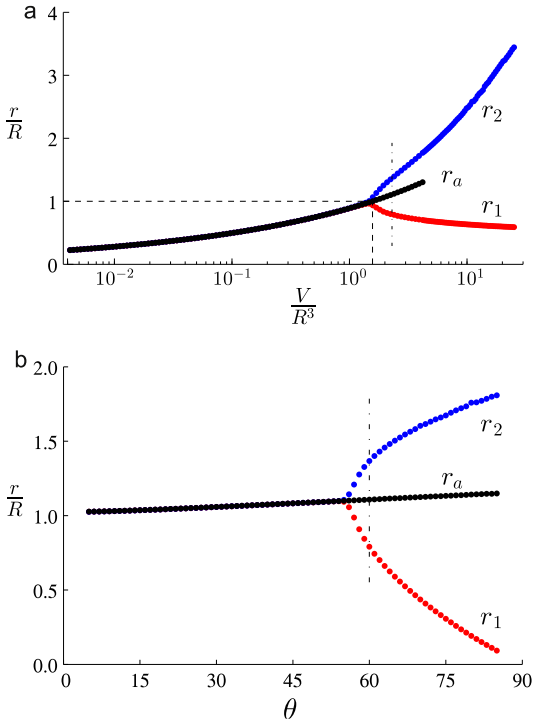

Fig. 5. Multiple simulations illustrate how the minimum radius r_1 and maximum radius r_2 compare to the axisymmetric radius r_a. (a) At fixed contact angle, the radii bifurcate at a critical volume. (b) At fixed volume, the radii bifurcate at a critical angle. The dashed lines depict the critical values and the dash-dotted lines intersect the points that correspond to Fig. 1d–e.

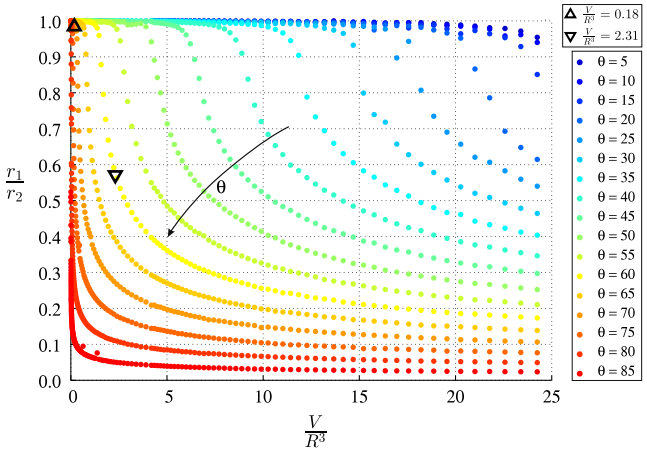

Fig. 6. The radius ratio r_1/r_2 as a function of bridge volume for various contact angles. The liquid bridge is axisymmetric when $r_1 = r_2$, and the triangles denote the experimental conditions in Fig. 1a and b.

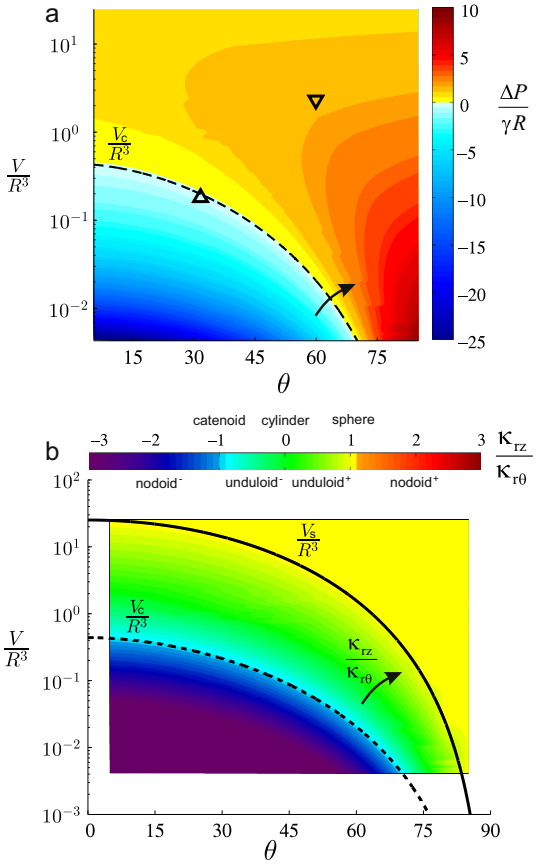

Fig. 7. The principle bridge curvatures indicate the internal pressure and shape of bridge. (a) Bridge capillary pressure is calculated from simulations with various volumes and contact angles. The simulations reveal a zero capillary pressure contour that is consistent with the exact solution for a catenoidal bridge between spheres (dashed line). The triangles locate the experimental conditions in Fig. 1, and the direction of the arrow indicates increasing capillary pressure. (b) The ratio of the principle curvatures provides insight into the shape of the bridge. Exact solutions for catenoidal and spherical bridges are plotted with a dashed and solid line respectively. All values beyond the range of the scalebar are depicted with the color of the extrema for clarity.

bridge surface (Fig. 1f). The capillary pressure inside the bridge can be related to these principle curvatures with $\Delta P = \gamma_{LV}(\kappa_{r\theta} + \kappa_{rz})$. For each contact angle $\theta < 90°$, there exists a volume V_c for which the bridge is a catenoid (see Appendix) and the capillary pressure changes sign. The catenoid volume for a given contact angle can be calculated analytically (Fig. 7a, dashed line), and the agreement with the sign change in the numerically calculated pressure provides further verification of the numerical model. It is interesting to note that the pressure monotonically increases as the contact angle increases for a given volume; yet, for a given contact angle, the pressure is non-monotonic as the volume changes.

Although it may be tempting to relate the sign change in Laplace pressure with the emergence of asymmetry, past studies have argued that axisymmetric bridges remain stable until the point in which they become spherical [22,23]. Indeed, we obtain further insight by plotting the ratio of the principle curvatures $\kappa_{rz}/\kappa_{r\theta}$ (Fig. 7b). Here a value of -1 corresponds to a catenoidal bridge, a value of 0 corresponds to a cylindrical bridge, and a value of 1 corresponds to a spherical bridge. Other values of this ratio signify that the bridge can be described by constant-mean-curvature surfaces referred to as unduloids and nodoids [1,6].

The noteworthy feature of Fig. 4b is that nodoidal bridges with positive curvatures $\kappa_{rz}/\kappa_{r\theta} > 1$ are absent. Fig. 1d illustrates such a shape, yet as expected this particular bridge is unstable to non-axisymmetric perturbations. For this particular volume and contact angle, the ratio of curvatures for the stable bridge is $\kappa_{rz}/\kappa_{r\theta} = 1$, suggesting that the asymmetric bridge shape is spherical. Indeed for each contact angle $\theta < 90°$, there exists a unique volume V_s for which an axisymmetric bridge is a spherical (solid line in Fig. 7b). All of the simulations conducted in which the volume of the bridge was greater than V_s, equilibrated to a spherical bridge shape with $\kappa_{rz}/\kappa_{r\theta} \approx 1$.

To highlight the importance of the spherical bridge, we rescale Fig. 5 so that the bridge volume is normalized by the axisymmetric spherical bridge volume V_s. With this scaling, all of the curves in Fig. 6 collapse together with $r_1/r_2 \approx 1$ when $V/V_s < 1$ (Fig. 8a). When $V/V_s > 1$, the ratio r_1/r_2 decreases and the bridge is no longer axisymmetric. Given the near collapse of the different contact angle simulations, it is natural to inquire whether analytic solutions to the asymmetry ratio r_1/r_2 are obtainable. We now solve for the exact solution by exploiting the rotational symmetries afforded by the solid spheres and the spherical bridge.

For every contact angle, there exists a spherical bridge with radius of curvature r_s and volume V_s [3,21]. For example, for $\theta = 60°$, the axisymmetric bridge is spherical only when $r_s = R$ and $V_s = \pi/2\ R^3$ (Fig. 8b). If the contact angle is fixed and bridge volume V increased, an axisymmetric constant-mean-curvature surface can be constructed, but it will no longer be spherical (Fig. 8c). Suppose that the solid spheres were not constrained to contact, but instead free to drift apart. The spheres would separate until the attractive force due to the line tension was exactly balanced by the repulsive capillary pressure. It has been proven in an axisymmetric configuration that these forces balance when the bridge is spherical [3,16]. The source of these forces is a potential reduction in surface energy, thus the minimum surface energy possible for a particular contact angle and volume is achieved when the spheres are separated by a distance $2d$ so that the resulting bridge is spherical (Fig. 8d). Because the spherical bridge is rotationally symmetric, one of the solid spheres could be rotated about the center of the bridge without modifying the surface areas A_{LG}, A_{SG}, and A_{SL} (Fig. 8e). Thus the solid spheres can be brought into contact while maintaining the minimized surface energy. Finally, the solid spheres can be rotated back to their original contacted alignment (Fig. 8f), revealing an asymmetric bridge configuration with a lower surface energy than the equivalent axisymmetric configuration (Fig. 8c). Although this argument illustrates that the total surface energy of the system would be reduced if it were able to satisfy the constraints and adopt a spherical shape, it does not rule out the possibility that a different non-axisymmetric shape

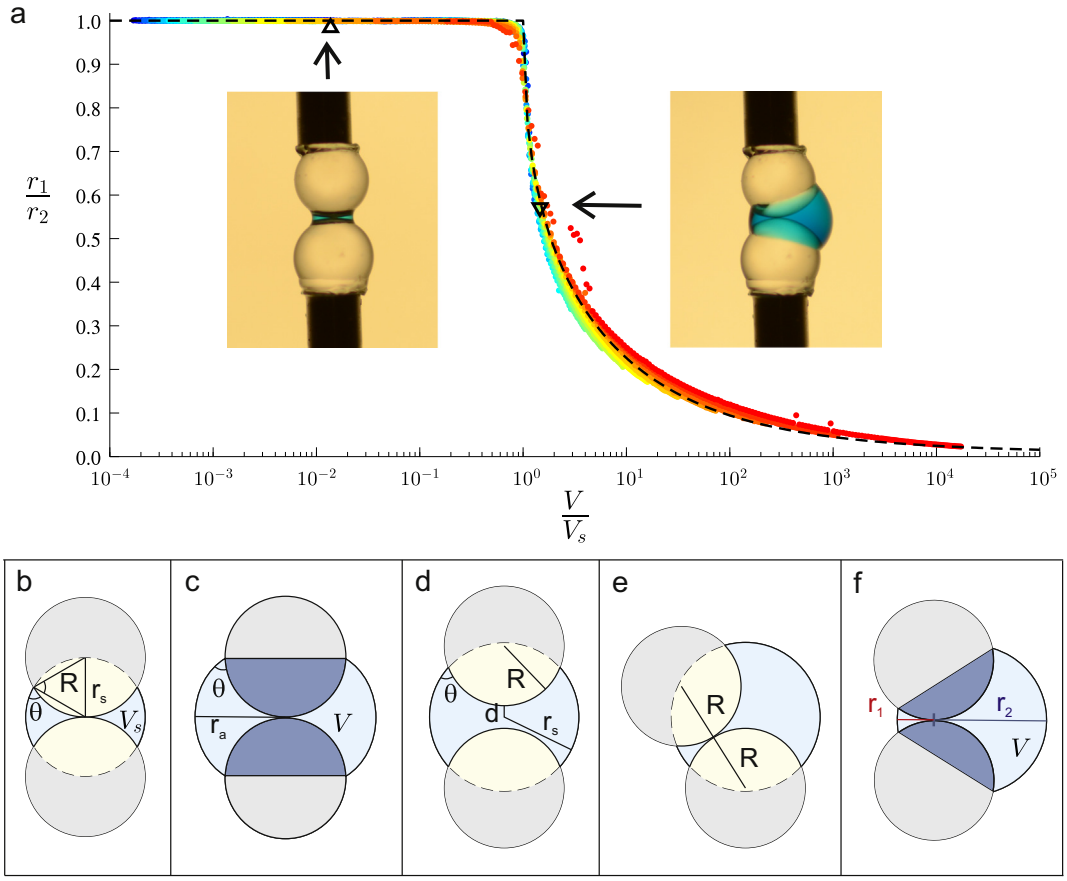

Fig. 8. Degree of asymmetry. (a) All the numerical data in Fig. 6 collapse on a master curve when the fluid volume V is normalized by the volume necessary to make a spherical bridge V_s. Triangles mark the experimental conditions and the dashed line denotes the exact solution, developed in text, when $\theta = 60°$. (b–f) Schematic drawings illustrating how one can arrive at an exact solution for part a.

could exist with a lower surface energy. Here our numerical results are vital, as they provide strong evidence that these axisymmetrically unstable bridges will reach a minimum energy state when they are spherical.

Thus from simple geometry, we conclude that the degree of asymmetry can be expressed as $\frac{r_1}{r_2} = 1$ when $V/V_s \leqslant 1$ and $\frac{r_1}{r_2} = \frac{r_s - \sqrt{(d+R)^2 - R^2}}{r_s + \sqrt{(d+R)^2 - R^2}} = \frac{1-\sqrt{\xi}}{1+\sqrt{\xi}}$ when $V/V_s \geqslant 1$, revealing that asymmetric morphology is controlled by a single parameter $\xi = 1 - 2\kappa_{r\theta} R \cos\theta$ (see Appendix). We have solved for values of this expression and these values agree well with the collapsed simulations (dashed line in Fig. 8a), as well as with the experimental water bridge illustrated in Fig. 1b (triangles in Fig. 8a).

4. Conclusions

In this paper, we numerically calculate the shape of the capillary bridge between two contacting spheres that minimizes the total surface energy for a given volume and contact angle. We find that the bridges adopt a non-axisymmetric shape if the volume of the liquid V is greater than volume required to form an axisymmetric spherical bridge V_s. Moreover, the numerical results provide evidence the minimum energy configuration is itself spherical so that the degree of asymmetry r_1/r_2 is controlled by a single parameter $\xi = 1 - 2\kappa_{r\theta} R \cos\theta$. Both the numeric simulations and our analysis demonstrate that the asymmetry does not require contact angle hysteresis to break the symmetry. In situations in which contact angle hysteresis is present, the equilibrium shapes that we compute should be identical in terms of the apparent contact angle provided that the contact line is not pinned. Indeed, apparent contact angles measured in our experimental observations likely deviate from the equilibrium contact angle; yet still, the resulting bridge shape is well-modelled upon specifying only the apparent contact angle and bridge volume.

This finding is relevant to a variety of applications that involve capillary bridges because the asymmetry we calculate affects both the shape and force of the bridge. Even though we have focused on the bridges between two identical spherical particles that are in contact, we anticipate that spherical bridges are a minimum energy configuration for separated spheres with various size and contact angles. Additionally, the results can be extended to predict the bridge shape when the contact angles are greater than 90°. In this case, $r_s < \sqrt{(d+R)^2 - R^2}$ so that r_1 is negative and the bridge no longer surrounds the origin. Finally, our findings have implications for the forces exerted onto the spheres from the capillary bridges. Our numerical results support the conclusion by Niven [23] that rather than exhibiting capillary repulsion when $V/V_s > 0$, the asymmetry in the bridge leads to no net capillary forces.

Acknowledgments

We are grateful to Weatherford Laboratories for financial support, and we thank Robin Hervé for early contributions to this project. We also thank Prof. Frieder Mugele for valuable discussions, alerting us to relevant past work, and sharing with us related

unpublished work that he and his colleagues are currently completing.

Appendix A. Exact solutions of capillary bridge profiles

A.1. Catenoidal bridge

The relationship between bridge volume V_{cat} and contact angle θ for a catenoidal profile between two solid spheres (Fig. A1) is determined by modifying a similar problem examined by Rubinstein and Fel [40]. After appropriate alterations and simplifications, we are left with a system of equations in three variables - dimensionless volume V_{cat}/R^3, contact angle θ, and filling angle ψ. The *filling angle* refers to the angle between the axis of symmetry and the contact line of the capillary bridge. An analytical solution may exist for this system; limited work was done simplifying it before resorting to a numerical solver.

$$t = \theta - \psi \tag{1}$$

$$C = \sin t \sin \psi \tag{2}$$

$$C \ln\left(\tan\frac{\theta}{2}\right) - \cos\psi + 1 = 0 \tag{3}$$

$$V_{cat}/R^3 = 2\pi C^3\left[\frac{\cos t}{\sin^2 t} + \ln\left(\cot\frac{t}{2}\right)\right] = -\frac{4}{3}\pi C^2(\cos^3\psi - 2\cos\psi + 2) \tag{4}$$

A.2. Cylindrical Bridge

For a cylindrical profile between two solid spheres (Fig. A2), solving the relationship between bridge volume V_{cyl} and contact angle θ is more straightforward than the catenoidal case. Unless otherwise stated, assume here and elsewhere that the solid spheres are in contact. For this special geometry, the contact and filling angles are complementary. The bridge volume is determined by subtracting spherical caps from a cylindrical volume of radius r and height h. A numerical solver is unnecessary in this case; a closed-form solution exists.

$$r_* = r/R = \cos\theta \tag{5}$$

$$h_* = h/R = 2(1 - \sin\theta) \tag{6}$$

$$V_{cap}/R^3 = \frac{1}{3}\pi\left(\frac{1}{2}h_*\right)^2\left(3 - \frac{1}{2}h_*\right) = \frac{1}{3}\pi(1 - \sin\theta)^2(2 + \sin\theta) \tag{7}$$

$$V_{cyl}/R^3 = \pi r_*^2 h_* - 2V_{cap}/R^3 = \frac{2}{3}\pi(1 - \sin\theta)(1 + \sin\theta - 2\sin^2\theta) \tag{8}$$

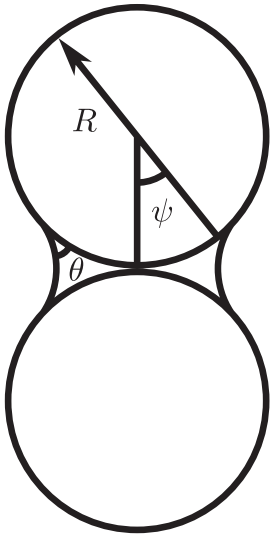

Fig. A1. Schematic drawing of a catenoidal liquid bridge between solid spheres.

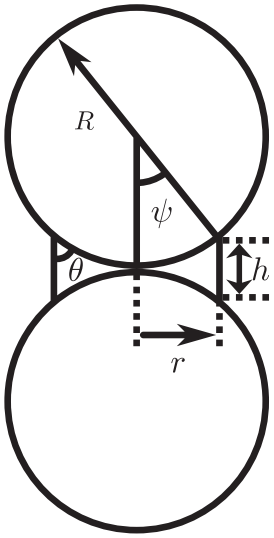

Fig. A2. Schematic drawing of a cylindrical liquid bridge between solid spheres.

A.3. Spherical bridge

The relationship between bridge volume V_s/R^3 and contact angle θ for a spherical profile between two solid spheres (Fig. A3) is determined by subtracting asymmetrical lenses from a spherical volume. The volume of these asymmetrical lenses is determined from the intersection of two spheres [41]. No numerical solving is needed here; a closed-form solution exists. In order to compare the behavior of this case with the solutions for catenoidal and cylindrical bridges, the solid spheres are assumed to remain in contact.

$$r_* = r_s/R = 2\cos\theta \tag{9}$$

$$V_{lens}/R^3 = \frac{1}{12}\pi r_*^3(8 - 3r_*) \tag{10}$$

$$V_s/R^3 = \frac{4}{3}\pi r_*^3 - 2V_{lens}/R^3 = \frac{1}{2}\pi r_*^4 = 8\pi\cos^4\theta \tag{11}$$

Shown in Fig. A4, the solutions profiles for catenoidal, cylindrical, and spherical bridges exhibit similar inverse relationships between bridge volume and contact angle. For spherical bridges,

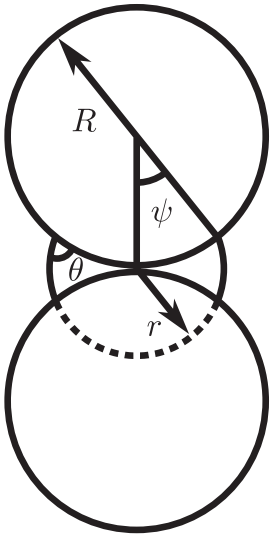

Fig. A3. Schematic drawing of a spherical liquid bridge between solid spheres.

this problem remains tractable even if a gap is added between the solid spheres. This family of solutions is examined later, since it is of interest when trying to predict the behavior of an unstable liquid bridge.

A.3. Spherical bridge (with gap)

Just as before, the relationship between bridge volume V_s/R^3 and contact angle θ is determined by subtracting asymmetrical lenses from a spherical volume. Now, however, we specify offset $\ell = R + d$ separating the solid spheres (Fig. A5). In the special case where the solid spheres are in contact, the offset is equal to sphere radius R.

$$r_* = r_s/R \tag{12}$$

$$\ell_* = \ell/R = \sqrt{r_*^2 - 2r_*\cos\theta + 1} \tag{13}$$

$$V_{lens}/R^3 = \frac{1}{12\ell_*}\pi(1 + r_* - \ell_*)^2\left(\ell_*^2 + 2\ell_* r_* - 3r_*^2 + 2\ell_* + 6r_* - 3\right) \tag{14}$$

$$\begin{aligned} V_s/R^3 &= \frac{4}{3}\pi r_*^3 - 2V_{lens}/R^3 \\ &= \frac{1}{6\ell_*}\pi\left(-\ell_*^4 + 6\ell_*^2 r_*^2 + 6\ell_*^2 - 8\ell_* + 3r_*^4 - 6r_*^2 + 3\right) \end{aligned} \tag{15}$$

As a final check, these equations reduce to Eqs. 9–11 in the limiting case where the gap between the solid spheres vanishes ($d = \ell - R = 0$).

In Fig. 8 of the main text, we plot r_1/r_2 as a function of V/V_s. As noted in the text,

$$\frac{r_1}{r_2} = \frac{r_s - \sqrt{(d+R)^2 - R^2}}{r_s + \sqrt{(d+R)^2 - R^2}} \tag{16}$$

which is equivalent to

$$\frac{r_1}{r_2} = \frac{1 - \sqrt{(\ell_*^2 - 1)/r_*^2}}{1 + \sqrt{(\ell_*^2 - 1)/r_*^2}} \tag{17}$$

Note that the expression can be written in terms of one variable

$$\xi = (\ell_*^2 - 1)/r_*^2 = 1 - \frac{2}{r_*}\cos\theta \tag{18}$$

Meanwhile, we can calculate the value of V/V_s that would correspond to a particular ℓ_* and θ by combining Eqs. (11) and (15)

$$V/V_s = \frac{1}{48\ell_*\cos^4\theta}\left(-\ell_*^4 + 6\ell_*^2 r_*^2 + 6\ell_*^2 - 8\ell_* + 3r_*^4 - 6r_*^2 + 3\right) \tag{19}$$

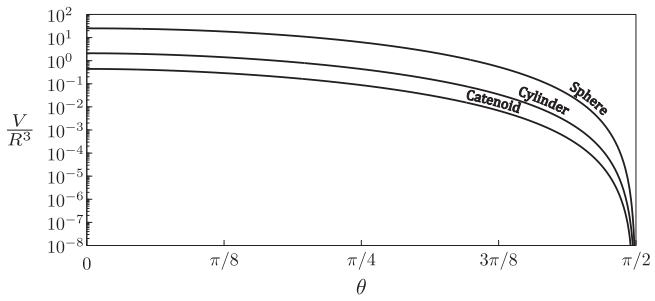

Fig. A4. Bridge volume V/R^3 as a function of contact angle θ for catenoidal, cylindrical, and spherical bridge profiles.

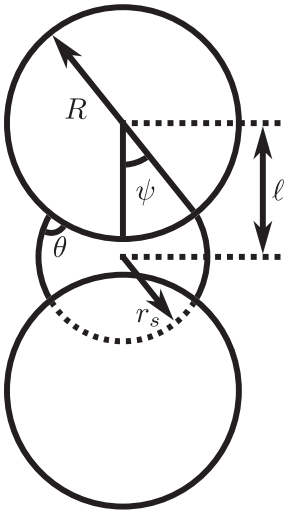

Fig. A5. Schematic drawing of a spherical liquid bridge between solid spheres with a gap.

By calculating corresponding values of $\frac{r_1}{r_2}$ and $\frac{V}{V_s}$ for various ξ, we produce the theoretical curve in Fig. 8 of the main text.

References

[1] C.H. Delaunay, J. Math. Pures Appl. 309–314 (1841).
[2] R. Finn, Math. Intelligencer 24 (2002) 21–33.
[3] F.M. Orr, L.E. Scriven, A.P. Rivas, J. Fluid Mech. 67 (1975) 723–742.
[4] P.G. De Gennes, F. Brochard-Wyart, D. Quéré, Capillarity and Wetting Phenomena: Drops, Bubbles, Pearls, Waves, Springer, 2004.
[5] H.J. Butt, M. Kappl, Adv. Colloid Interface Sci. 146 (2009) 48–60.
[6] J.B. Bostwick, P.H. Steen, Annu. Rev. Fluid Mech. 47 (2015) 539–568.
[7] L. Bocquet, E. Charlaix, S. Ciliberto, J. Crassous, Nature 396 (1998) 735–737.
[8] E. Koos, N. Willenbacher, Science 331 (2011) 897–900.
[9] W. Haines, J. Agr. Sci. 15 (1925) 529–535.
[10] R.A. Fisher, J. Agr. Sci. 16 (1926) 492–505.
[11] N.R. Morrow, Interfacial Phenomena in Petroleum Recovery, CRC Press, 1990.
[12] P. York, J. Pharm. Sci. 64 (1975) 1216–1221.
[13] T.C. Halsey, A.J. Levine, Phys. Rev. Lett. 80 (1998) 3141.
[14] M. Scheel, R. Seemann, M. Brinkmann, M. Di Michiel, A. Sheppard, B. Breidenbach, S. Herminghaus, Nat. Mater. 7 (2008) 189–193.
[15] J. Plateau, Statique expérimentale et théorique des liquides soumis aux seules forces moléculaires, Gauthier-Villars, 1873.
[16] G. Mason, W. Clark, Brit. Chem. Eng. 10 (1965) 327–328.
[17] G. Lian, C. Thornton, M.J. Adams, J. Colloid Interface Sci. 161 (1993) 138–147.
[18] C.D. Willett, M.J. Adams, S.A. Johnson, J.P. Seville, Langmuir 16 (2000) 9396–9405.
[19] Y.I. Rabinovich, M.S. Esayanur, B.M. Moudgil, Langmuir 21 (2005) 10992–10997.
[20] D. Megias-Alguacil, L.J. Gauckler, AIChE J. 55 (2009) 1103–1109.
[21] B.Y. Rubinstein, L.G. Fel, J. Colloid Interface Sci. 417 (2014) 37–50.
[22] T.I. Vogel, Pac. J. Math. 2 (2006) 367–377.
[23] R.K. Niven, J. Pet. Sci. Eng. 52 (2006) 1–18.
[24] R.N. Wenzel, Ind. Eng. Chem. 28 (1936) 988–994.
[25] A.B.D. Cassie, S. Baxter, Trans. Faraday Soc. 40 (1944) 546–551.
[26] J.F. Joanny, P.G. de Gennes, J. Chem. Phys. 81 (1984) 552.
[27] E.A. Bormashenko, Wetting of Real Surfaces (de Gruyter, 2013).
[28] M.J. Russo, P.H. Steen, J. Colloid Interface Sci. 113 (1986) 154–163.
[29] N.A. Bezdenejnykh, J. Meseguer, J.M. Perales, Phys. Fluids A 4 (1992) 677–680.
[30] J. Meseguer, L.A. Slobozhanin, J.M. Perales, Adv. Space Res. 16 (1995) 5–14.
[31] N.K. Adam, J. Soc. Dyers Colour. 53 (1937) 121–129.
[32] B.J. Carroll, Langmuir 2 (1986) 248–250.
[33] G. McHale, M.I. Newton, B.J. Carroll, Oil Gas Sci. Technol. 56 (2001) 47–54.
[34] G. McHale, M.I. Newton, Colloids Surf. A 206 (2002) 79–86.
[35] H.B. Eral, J. de Ruiter, R. de Ruiter, J.M. Oh, C. Semprebon, M. Brinkmann, F. Mugele, Soft Matter 7 (2011) 5138–5143.
[36] K.A. Brakke, Exper. Math. 1 (1992) 141–165.
[37] K.A. Brakke, Surface Evolver Manual, 2013.
[38] G. Taubin, IEEE Trans. Pattern Anal. Mach. Intell. 13 (1991) 1115–1138.
[39] E.A. Bormashenko, J. Phys. Chem. C 113 (2009) 17275–17277.
[40] B.Y. Rubinstein, L.G. Fel, Theory of Pendular Rings Revisited. arXiv:1207.7096v1, 2012.
[41] Eric W. Weisstein, "Sphere-Sphere Intersection" From MathWorld – A Wolfram Web Resource, 2013. <http://mathworld.wolfram.com/Sphere-SphereIntersection.html>.